# Reactive Molecular Dynamics Insights into Hydrogen and Carbon Co-production from Methane and Propane Pyrolysis

Yuan Tian[a,b*], Nathalie De Geyter[b], Carla Bittencourt[a], Chris Ewels[c], Rony Snyders[a,d]

[a] Research Group ChIPS, Department of Chemistry, University of Mons, 20 Place du Parc, 7000 Mons, Belgium

[b] Research Unit Plasma Technology (RUPT), Department of Applied Physics, Ghent University, Sint-Pietersnieuwstraat 41 B4, 9000 Ghent, Belgium

[c] Nantes Université, CNRS, Institut des Matériaux Jean Rouxel, IMN, F-44000, Nantes, France

[d] Materia Nova Research Center, 3 Avenue Copernic, 7000 Mons, Belgium

Corresponding author: Yuan Tian; Email: Yuan.Tian@umons.ac.be

Abstract: This study investigates the pyrolysis behavior of methane ($CH_4$) and propane ($C_3H_8$) under high-temperature and high-density conditions using reactive molecular dynamics (ReaxFF-MD) simulations, with particular emphasis on the co-production of hydrogen ($H_2$) and carbon-based by-products. The results show that $C_3H_8$ decomposes more rapidly than $CH_4$ under similar conditions, primarily because its weaker C–C bonds have a lower activation energy for bond cleavage. In both systems, $H_2$ is primarily produced via hydrogen abstraction reactions involving H radicals formed in earlier stages of the process. Acetylene ($C_2H_2$) arises through the stepwise dehydrogenation of $C_2$ species. $H_2$ production progressively increases with pyrolysis time in both systems, driven by entropy effects. Notably, $CH_4$ yields more $H_2$ in the initial phase due to the early abundance of H radicals, whereas $C_3H_8$ exhibits a slower initial $H_2$ yield. Similarly, $C_2H_2$ formation in the $CH_4$ system requires more reaction steps, while $C_3H_8$ rapidly forms $C_2H_5$ intermediates that facilitate faster $C_2H_2$ generation, resulting in faster carbon condensation during $C_3H_8$ pyrolysis. The formation of carbon clusters proceeds through three distinct stages: feedstock fragmentation, carbon chain growth, and carbon cluster aromatization/graphitization. The final stage is characterized by the elimination of hydrogen and the formation of six-membered aromatic rings. In addition, the study provides a detailed analysis of the carbon nucleation process, suggesting that the Polycyclic Aromatic Hydrocarbon (PAH) model is likely more applicable at low densities and temperatures. In contrast, the polyyne model tends to dominate under high-density and high-temperature conditions. Overall, this study offers atomic-level insights into the pyrolysis of light hydrocarbons, highlighting the utility of ReaxFF-MD simulations in unraveling complex, coupled gas-phase and condensation kinetics.

Key words: Methane and propane pyrolysis, $H_2$ production, carbon formation, ReaxFF-MD.

## 1. Introduction

Hydrogen ($H_2$), as an important industrial feedstock and clean energy carrier, is expected to play an increasingly important role in meeting the rising global energy demand and facilitating the transition toward a low-emission energy landscape in the coming decades.[1,2] Currently, however, more than 99% of $H_2$ is produced from fossil fuels without carbon reduction measures.[2] To meet decarbonization targets, the development and implementation of low-emission $H_2$ production technologies is essential. Among these, hydrocarbon pyrolysis stands out as a promising approach, as it enables the generation of $CO_2$-free $H_2$ while simultaneously producing solid carbon. This carbon by-product offers a sustainable alternative to conventional carbon black, which is typically manufactured through high-emission, incomplete combustion processes.[3-6] This dual advantage of avoiding direct $CO_2$ emissions and creating valuable carbon materials enhances both the environmental and economic appeal of pyrolysis-based $H_2$ production.

Studies on hydrocarbon pyrolysis typically rely on a multifaceted experimental and theoretical framework to elucidate its complex reaction pathways and the formation of diverse products. Conventional analytical techniques, such as gas chromatography (GC) and mass spectrometry (MS), are employed to quantify feedstock conversion and characterize the distribution of gaseous

products.[7-9] To examine the morphology and structure of the solid carbon produced, advanced characterization methods, including transmission electron microscopy (TEM), X-ray diffraction (XRD), and Raman spectroscopy, are widely employed.[10-15] For kinetic studies, shock tube experiments provide quantitative measurements of reaction rate constants, essential data for the development and validation of kinetic models.[16-22] Complementarily, laser diagnostics enable the spatially and temporally resolved detection of short-lived radicals and soot particles, as well as precise measurements of physical parameters such as gas temperature and density,[23-25] thereby offering critical insights into reaction kinetics. In addition, ab initio calculations are employed to probe key elementary reactions, such as hydrogen abstraction and aromatic ring formation, providing theoretical insights into the construction of the corresponding potential energy surfaces.[26-29] Despite notable progress, fundamental challenges persist in achieving a comprehensive characterization of hydrocarbon pyrolysis systems. Short-lived radicals and reactive intermediates that govern pyrolysis pathways are difficult to detect using conventional GC/MS techniques.[30] Carbon characterization methods provide only post-reaction snapshots of the solid phase and are unable to capture the real-time dynamics of carbon growth. Kinetic models often rely on simplified reaction pathways and tend to overlook complex interactions in multi-component systems or heterogeneous reactions.[31] Laser diagnostics, while powerful, are constrained by spectral interference and a limited range of detectable species, reducing their effectiveness in complex pyrolysis environments.[32] Additionally, ab initio methods are typically restricted to simulations involving only a few hundred atoms over picosecond timescales, which limits the capture of larger-scale or longer-time dynamics.[31] Collectively, these limitations hinder the development of a comprehensive mechanistic understanding of hydrocarbon pyrolysis.

To address these limitations, reactive force field molecular dynamics (ReaxFF-MD) offers a powerful approach for directly tracking bond-breaking and bond-forming events without relying on predefined reaction pathways.[33,34] ReaxFF-MD is particularly well suited for studying pyrolysis systems involving carbon formation, as it can simultaneously capture gas-phase radical chemistry, surface reactions, and solid-phase nucleation at the atomic scale. This versatility has made ReaxFF-MD highly effective in studies of hydrocarbon pyrolysis, combustion processes, and the synthesis of carbon nanomaterials,[35-45] serving as a valuable complement to both experimental techniques and ab initio calculations. ReaxFF-based investigations of light hydrocarbon pyrolysis have been conducted for various feedstocks, including methane ($CH_4$),[41-42] ethane ($C_2H_6$) and acetylene ($C_2H_2$),[43-44] and butane ($C_4H_{10}$).[45] While these studies have provided valuable insights into hydrocarbon decomposition mechanisms and certain aspects of carbon formation, detailed analyses of carbon formation—especially the nucleation stage—are still lacking. Additionally, the formation pathways and roles of key products, particularly $H_2$ and $C_2H_2$, remain insufficiently explored. This study aims to address these gaps by conducting a comparative analysis of $CH_4$ and propane ($C_3H_8$) pyrolysis.

Among various hydrocarbon feedstocks, $CH_4$ and $C_3H_8$ are particularly attractive for pyrolysis research due to their industrial relevance. $CH_4$, the simplest hydrocarbon and a representative C1 compound, possesses the highest H/C ratio and is the primary component of natural gas, making it a key feedstock for $H_2$ production. Its molecular simplicity and abundance, therefore, render it an ideal model system for exploring the fundamental chemistry of C1 pyrolysis. $C_3H_8$, a C3 hydrocarbon and a major constituent of liquefied petroleum gas (LPG), offers distinct practical advantages, including liquid-phase feedstock, higher energy density, and favorable storage and transportation properties.[13] Focusing strategically on these C1 and C3 hydrocarbons enables a systematic comparative analysis of $H_2$ production and carbon formation dynamics, thereby linking mechanistic insights with practical energy applications.

In this study, ReaxFF-MD simulations were performed to investigate the pyrolysis behavior of $CH_4$ and $C_3H_8$ under high-temperature and high-density conditions. The analysis starts with the decomposition kinetics of both feedstocks, identifying their main fragmentation pathways. Subsequently, the time evolution of key gaseous species is examined with particular attention to the mechanisms governing $H_2$ and $C_2H_2$ formation. Finally, the focus was shifted to the formation of carbon clusters, culminating in a comprehensive discussion of the carbon nucleation mechanisms revealed by ReaxFF. This work complements our ongoing research on plasma-based light hydrocarbon pyrolysis, providing detailed insights into the thermal decomposition mechanisms that underpin the plasma process.

## 2. Computational methods

### *2.1 Overview of ReaxFF*

ReaxFF is designed to accurately simulate chemical reactions and interactions using a bond order (BO)-based approach. The

total energy of the system is expressed as the sum of several partial energy contributions, as shown in equation (1):

$$E_{system} = E_{bond} + E_{over} + E_{under} + E_{val} + E_{pen} + E_{tors} + E_{conj} + E_{vdWaals} + E_{Coulomb} \quad (1)$$

in which $E_{bond}$ represents the bond energy, while $E_{over}$ and $E_{under}$ denote the energy contributions from over-coordinated and under-coordinated atoms, respectively. The terms $E_{val}$, $E_{pen}$, $E_{tors}$, and $E_{conj}$ correspond to the valence angle value, penalty energy, torsion energy, and conjugation effects to the molecular energy, respectively. Additionally, $E_{vaWaals}$ and $E_{Coulomb}$ represent the non-bonded van der Waals interactions and Coulomb interactions. For a more detailed description of the ReaxFF methodology, readers are referred to prior foundational studies.[33,34]

*2.2 Simulation details*

Configuration details of the simulation setup are provided in Fig. 1 and Table 1. All simulations were conducted using the open-source Large-scale Atomic/Molecular Massively Parallel Simulation (LAMMPS) package,[46] employing the CHO-2016 parameter set.[40] This parameter set has already been applied in the simulations of different hydrocarbon fuels, including $CH_4$, syngas, $C_2H_2$, and JP-10.[35-40] The simulations were carried out in the NVT ensemble, maintaining constant atom number, volume, and temperature, with a damping coefficient of 100 fs controlled via a Berendsen thermostat.[40] NVT was selected over NPT (constant pressure rather than volume) due to the inherent difficulty of maintaining stable pressure in the simulation box and the relatively minor influence of pressure compared to temperature on pyrolysis behavior. Periodic boundary conditions were applied in all three spatial directions.

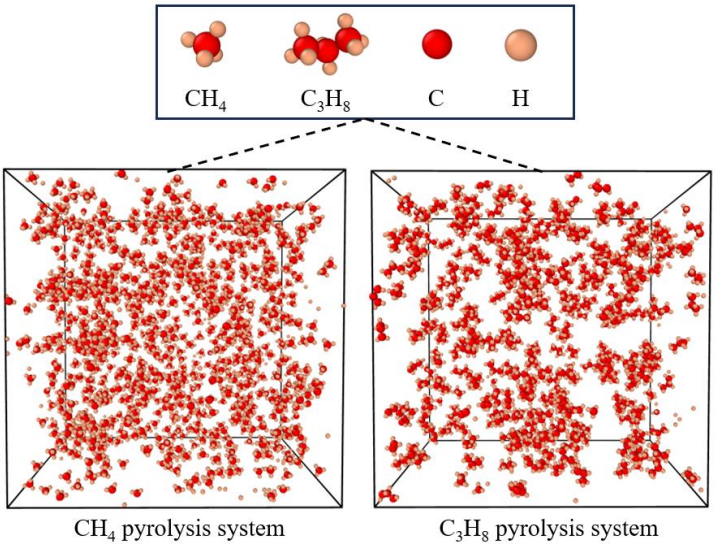


Fig. 1. Pyrolysis models for ReaxFF-MD simulations.

Table 1. Simulation conditions.

| Feedstock | Case | Number | Temperature (K) | Density (g/cm$^3$) | Box size* (Å) |
|---|---|---|---|---|---|
| $CH_4$ | 1 | 1000 | 2500 | 0.1 | 64.3 |
| | 2 | 1000 | 2750 | 0.1 | 64.3 |
| | 3 | 1000 | 3000 | 0.1 | 64.3 |
| | 4 | 1000 | 3250 | 0.1 | 64.3 |
| | 5 | 1000 | 3500 | 0.1 | 64.3 |
| $C_3H_8$ | 1 | 333 | 2500 | 0.1 | 62.5 |
| | 2 | 333 | 2750 | 0.1 | 62.5 |
| | 3 | 333 | 3000 | 0.1 | 62.5 |
| | 4 | 333 | 3250 | 0.1 | 62.5 |
| | 5 | 333 | 3500 | 0.1 | 62.5 |

* The box size corresponds to the edge length of the cubic simulation cell.

BO cut-off values were set to 0.55 for C-C, 0.4 for C-H, and 0.55 for H-H atomic pairs.[42]

All atoms were initially equilibrated at 300 K for 100 ps to eliminate memory effects from the initial configurations, during which no decomposition of the feedstocks was observed prior to heating to the target temperatures. Following equilibration, production runs were carried out for 5 ns in the case of $CH_4$ pyrolysis and 2 ns for $C_3H_8$ pyrolysis. A time step of 0.1 fs was used to integrate Newton's equations of motion via the velocity-Verlet algorithm. Atomic coordinates were recorded every 1 ps for subsequent trajectory analysis. Visualization and post-simulation analyses were conducted using OVITO and custom Python scripts.[47] To analyze reaction pathways, the ReactNetGenerator tool was employed.[48]

The computationally accessible timescales in ReaxFF-MD simulations are limited to the nanosecond regime, significantly shorter than those encountered in experimental studies. To overcome this limitation and capture chemically relevant events within a tractable computational timeframe, simulations were performed at elevated temperatures to accelerate reaction kinetics, thereby increasing the frequency of reactive collisions, as documented in previous studies.[35-45] Additionally, the system density was increased to further increase collision frequency, resulting in initial pressures approximately three orders of magnitude higher than atmospheric pressure.[35-45] Prior studies have reported that $CH_4$ fragmentation behavior is largely unaffected by density, with temperature being the dominant factor influencing $CH_4$ pyrolysis.[41,42] Accordingly, the density in this study was fixed at 0.1 g/cm³, and the temperature was varied solely. To ensure statistical reliability, three independent simulation replicates were performed under each condition.

## 3. Results and discussion

### *3.1. Kinetic analysis of feedstock decomposition*

To characterize the decomposition kinetics of $CH_4$ and $C_3H_8$ across different temperatures, five simulation cases were analyzed using data collected over 1000 ps for $CH_4$ and 500 ps for $C_3H_8$, as shown in Fig. 2. The results indicate that the decomposition rates of both $CH_4$ and $C_3H_8$ increase with temperature, as higher temperatures provide more kinetic energy for molecules to help them overcome the activation energy barriers. Moreover, $C_3H_8$ decomposes significantly faster than $CH_4$, as evidenced by the faster decomposition of $C_3H_8$ molecules under identical conditions. To quantitatively assess the decomposition kinetics and support subsequent analysis, Arrhenius parameters were extracted by fitting the reactant-loss profiles to a first-order kinetic model, a methodology widely adopted in both experimental and computational studies of fuel pyrolysis.[18-22,35] The apparent rate constant at each temperature was determined by fitting the reactant-loss data to an exponential decay function, as described by Equation (2),

$$N_t = N_0 \exp(-kt) \qquad (2)$$

where $N_0$ is the initial number of feedstock molecules in the system, $N_t$ is the number of molecules at any given time *t*, and *k* is the apparent rate constant. The obtained apparent rate constants were subsequently used to construct Arrhenius plots, from which the activation energy ($E_a$) was extracted using the Arrhenius equation:

$$k = Ae^{\frac{-E_a}{RT}} \qquad (3)$$

here, $R$ is the universal gas constant (8.314 J·mol$^{-1}$ K$^{-1}$) and $T$ is the absolute temperature in Kelvin. The natural logarithm of the apparent reaction rate constant ($lnk$) obtained from the simulations was plotted against the inverse temperature ($1/T$) to generate the Arrhenius plots shown in Figs. 2b and 2d. It is observed that the first-order kinetics are well-described by a single Arrhenius function, yielding activation energies of 413 kJ/mol for $CH_4$ and 266 kJ/mol for $C_3H_8$.

To investigate the initial decomposition mechanisms, early-stage reaction networks were analyzed at 3500 K over 250 ps for $CH_4$ and 50 ps for $C_3H_8$, as most feedstock dissociation occurs within these timeframes. The primary decomposition pathways for both $CH_4$ and $C_3H_8$ are summarized in Table 2, with reactions and their corresponding frequencies obtained using the ReactNetGenerator tool.[48]

For $CH_4$, the initial decomposition step involves the cleavage of a C–H bond (reaction (2)), which requires overcoming an energy barrier of approximately 462 kJ/mol.[41] The resulting H radicals can subsequently abstract H atoms from intact $CH_4$ molecules at a significantly higher reaction rate (reaction (1)), due to the lower activation energy associated with the hydrogen abstraction process. Both experimental and ab initio studies have investigated the rate constants for this reaction, consistently reporting an activation energy of approximately 56 kJ/mol.[26-28] This value is markedly lower than that of direct C–H bond dissociation and reaction (1); therefore, it accounts for roughly 44.4% of the overall $CH_4$ decomposition pathway.

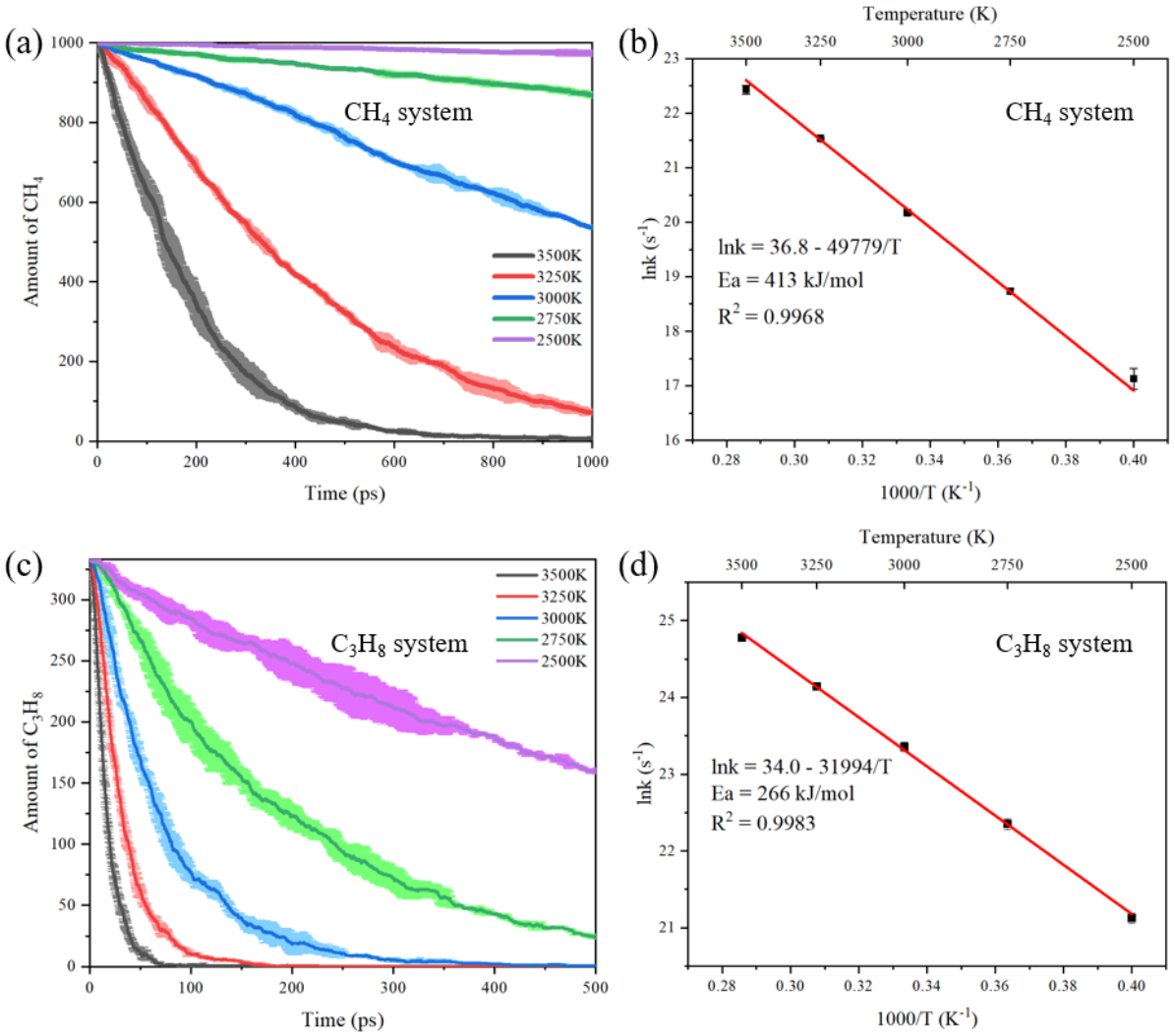


Fig. 2. (a) $CH_4$ consumption observed in ReaxFF-MD simulations at various temperatures, and (b) the corresponding Arrhenius plot of *lnk* versus *1/T*. (c) $C_3H_8$ consumption observed in ReaxFF-MD simulations at various temperatures, and (d) the corresponding Arrhenius plot of *lnk* versus *1/T*. The lines represent the averaged values obtained from three simulations, and the shaded areas around the lines indicate the corresponding error bars, reflecting the variability of the data. This convention is applied consistently to all figures throughout the manuscript.

Unlike $CH_4$, the initial dissociation of $C_3H_8$ can proceed via cleavage of either a C–C or C–H bond, with corresponding bond dissociation energies of approximately 352 kJ/mol and 420 kJ/mol, respectively.[18,49] Among these pathways, C–C bond cleavage (reaction (4)) dominates during the early stages of $C_3H_8$ decomposition, accounting for roughly 49.5% of the initial reactions. This highlights its critical role in the onset of $C_3H_8$ pyrolysis.[18,22] In contrast, C–H bond cleavage (reaction (6)) contributes less significantly to $C_3H_8$ decomposition due to its higher energetic requirement. Hydrogen abstraction from $C_3H_8$ (reaction (5)) also plays an important role, facilitated by its relatively low activation energy. However, this pathway depends on the presence of H radicals, which are typically generated via initial C–H bond dissociation involving a higher energy barrier, as mentioned earlier.

Table 2. The top three decomposition reactions and their net reaction frequency at 3500 K.

| | Reactions | Frequency |
|---|---|---|
| (1) | $H + CH_4 \rightarrow CH_3 + H_2$ | 44.4% |
| (2) | $CH_4 \rightarrow CH_3 + H$ | 22.6% |
| (3) | $CH_4 + CH_4 \rightarrow 2CH_3 + H_2$ | 5.4% |
| (4) | $C_3H_8 \rightarrow CH_3 + C_2H_5$ | 49.5% |
| (5) | $H + C_3H_8 \rightarrow H_2 + C_3H_7$ | 10.8% |
| (6) | $C_3H_8 \rightarrow H + C_3H_7$ | 8.1% |

Consequently, hydrogen abstraction plays a less dominant role in the early stages of $C_3H_8$ decomposition compared to $CH_4$, where H radical generation and subsequent abstraction occur more readily. The combined contributions of these reaction channels result in an apparent activation energy of approximately 266 kJ/mol for $C_3H_8$ decomposition. Notably, this value closely aligns with the C–C bond dissociation energy, supporting the conclusion that C–C bond cleavage serves as the rate-limiting step in $C_3H_8$ decomposition.[22]

In contrast, the overall activation energy for $CH_4$ decomposition is determined to be approximately 413 kJ/mol, which is in good agreement with previously reported values ranging from 326 to 423 kJ/mol.[50] This consistency between literature data and the results obtained from ReaxFF-MD simulations further validates the accuracy and reliability of the ReaxFF approach for modeling hydrocarbon decomposition processes.

*3.2. Gaseous products analysis*

To facilitate comparison with experimental studies, $H_2$ selectivity is evaluated using the H atom balance. This metric provides insight into the efficiency of $H_2$ generation and is calculated using Equation (4):

$$S_{H_2} = \frac{C_{H_2}}{C_{converted} \times R_H} \times 100\% \quad (4)$$

Here, $C_{H_2}$ represents the number of produced $H_2$ molecules, $C_{converted}$ is the number of feedstock molecules that have undergone decomposition, and $R_H$ is the theoretical maximum number of $H_2$ molecules that can be generated from the complete decomposition of a single feedstock molecule. For $CH_4$ and $C_3H_8$, $R_H$ corresponds to 2 and 4, respectively.

Similarly, the selectivity of $C_2H_2$ is evaluated for several reasons: (i) it is a key gaseous product formed during the pyrolysis of both $CH_4$ and $C_3H_8$, (ii) it serves as an important industrial feedstock with broad applications,[51] and (iii) its formation is closely associated with the initial stages of carbon formation and growth in both combustion and pyrolysis environments.[3,30] The selectivity of $C_2H_2$ is quantified based on the carbon atom balance, as defined in Equation (5):

$$S_{C_2H_2} = \frac{C_{C_2H_2}}{C_{converted} \times R_C} \times 100\% \quad (5)$$

where $C_{C_2H_2}$ is the number of $C_2H_2$ molecules formed, and $R_C$ is the theoretical maximum number of $C_2H_2$ molecules that can be generated from the complete decomposition of a single feedstock molecule. For $CH_4$ and $C_3H_8$, $R_C$ corresponds to 0.5 and 1.5, respectively.

Fig. 3 illustrates the time evolution of $H_2$ and $C_2H_2$ selectivity during the pyrolysis of $CH_4$ and $C_3H_8$. In the $CH_4$ pyrolysis system, the $H_2$ selectivity initially exhibits a lower limit of approximately 25% (Fig. 3a). This value can be rationalized by considering the primary decomposition reactions of $CH_4$, as shown in Table 2. The initial dissociation of $CH_4$ involves C–H bond cleavage, yielding a H radical and a methyl radical ($CH_3$). The H radical can subsequently abstract a hydrogen atom from another $CH_4$ molecule, producing a $H_2$ molecule (a fast reaction due to the low activation energy barrier). Alternatively, two $CH_4$ molecules can form one $H_2$ molecule and two $CH_3$ molecules, leading to a theoretical initial $H_2$ selectivity of 25%. As time progresses, additional C–H bond cleavages and successive hydrogen-abstraction reactions release additional H radicals from various intermediate species, thereby increasing overall $H_2$ selectivity. This trend can be attributed to entropy effects, since the increase in the number of $H_2$ molecules lowers the Gibbs free energy of the system at elevated temperatures.[52]

In contrast to $H_2$, the selectivity of $C_2H_2$ exhibits a markedly different trend. As shown in Fig. 3b, no $C_2H_2$ formation is observed at low temperatures. Theoretically, the formation pathway of $C_2H_2$ is considerably more complex than that of $H_2$. While $H_2$ formation primarily involves the generation of H radicals followed by hydrogen abstraction reactions, the formation of $C_2H_2$ requires multiple steps, as reported in previous work.[53] Initially, $CH_4$ must undergo C–H bond cleavage to generate $CH_3$ radicals. Two $CH_3$ radicals can subsequently recombine to form $C_2H_6$, which then undergoes a series of dehydrogenation reactions to yield $C_2H_2$ ultimately. This multistep process requires longer reaction times, which explains the temperature threshold required for observable $C_2H_2$ formation within the simulation timeframe.

In the $C_3H_8$ pyrolysis system, the initial $H_2$ selectivity is markedly lower than that observed in $CH_4$ pyrolysis (Fig. 3c). This difference arises from the dominant decomposition pathway of $C_3H_8$, which primarily proceeds through C–C bond cleavage. Notably,

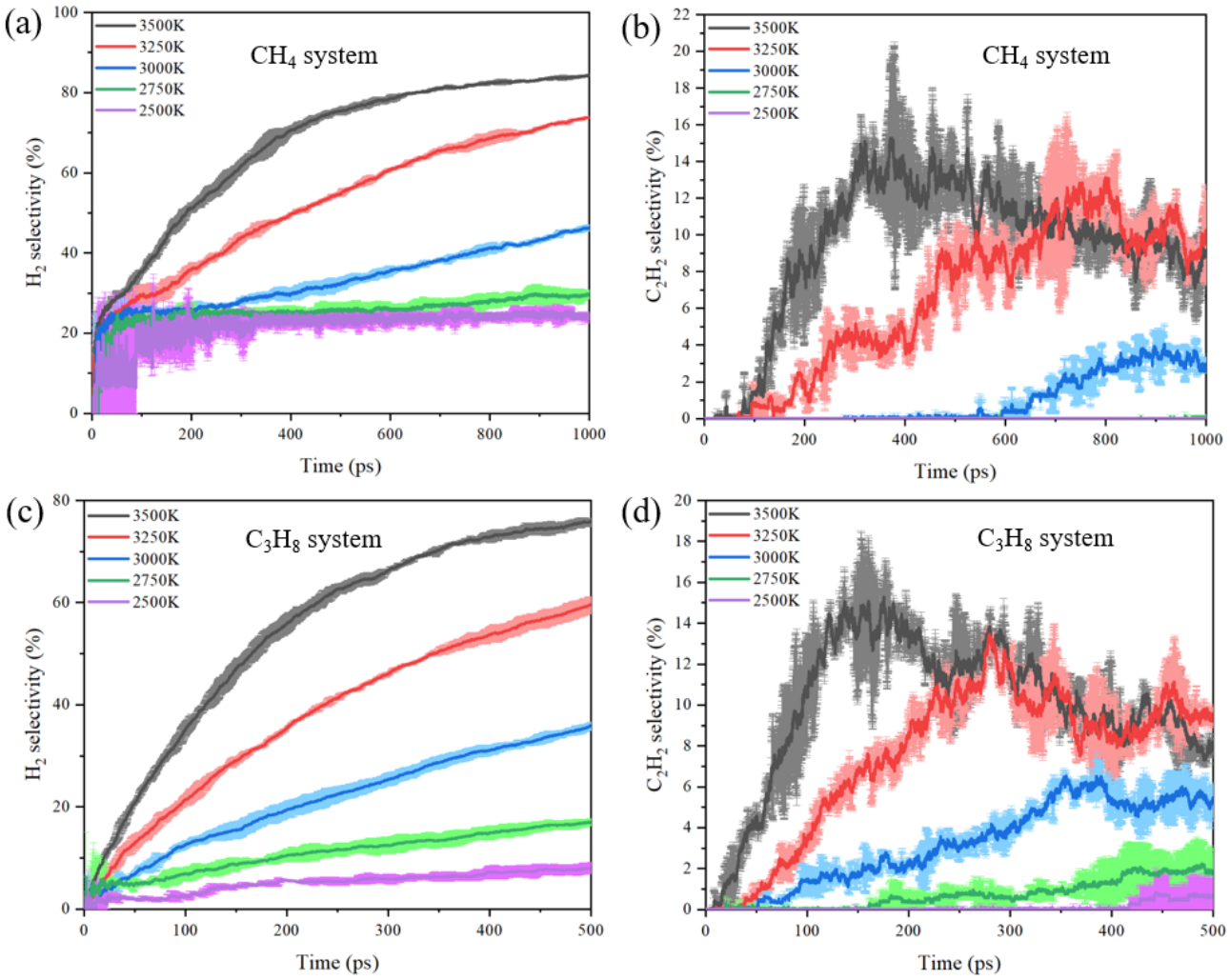


Fig. 3. Time evolution of $H_2$ and $C_2H_2$ selectivity during $CH_4$ and $C_3H_8$ pyrolysis as a function of time for different pyrolysis temperatures. (a) $H_2$ selectivity in $CH_4$ system; (b) $C_2H_2$ selectivity in $CH_4$ system; (c) $H_2$ selectivity in $C_3H_8$ system; (d) $C_2H_2$ selectivity in $C_3H_8$ system.

this pathway does not directly yield H radicals, thereby limiting the occurrence of immediate hydrogen abstraction reactions that drive early $H_2$ formation. As a result, $H_2$ selectivity in $C_3H_8$ increases gradually over time. In contrast, the formation of $C_2H_2$ (Fig. 3d) during $C_3H_8$ pyrolysis requires fewer reaction steps, since the $C_2H_5$ radical is directly produced through the initial dissociation of $C_3H_8$. This pathway is considerably more efficient than the multi-step generation of $C_2H_5$ in $CH_4$ pyrolysis, which explains the earlier appearance of $C_2H_2$ in the $C_3H_8$ system compared with the $CH_4$ system under identical conditions. Based on the above mechanistic analysis, the reaction pathways for $H_2$ and $C_2H_2$ generation are summarized in Fig. 4.

To provide a comprehensive overview of the species evolution over time in both pyrolysis systems, the time-dependent amounts of carbon-containing species (up to C7) and $C_2H_x$ species are presented in Fig. 5, where CX denotes all species containing X carbon atoms (X = 1, 2, …7). The C1-C7 species represent small hydrocarbon fragments commonly generated during the activation of premixed hydrocarbon fuels,[54] while the $C_2H_x$ species correspond to key intermediates involved in the formation of $C_2H_2$. As shown in Fig. 5a, all species exhibit a characteristic rise followed by a decline in concentration, indicating their role as transient intermediates during pyrolysis. Additionally, the time at which peak concentrations occur increases with carbon number, suggesting that smaller carbon-containing species act as precursors to larger ones through addition reactions.

Fig. 5b illustrates the evolution of C2 species in the $CH_4$ pyrolysis system. The concentration of $C_2H_6$ rises initially, driven by the early formation of $CH_3$ radicals following $CH_4$ decomposition. Subsequently, through a series of dehydrogenation reactions, $C_2H_6$ is progressively converted into $C_2H_5$, $C_2H_4$, $C_2H_3$, and ultimately $C_2H_2$, as evidenced by the transient accumulation and subsequent depletion of these intermediate species. This behavior further supports the $C_2H_2$ formation pathways proposed in Fig. 4.

At later stages, the $C_2H$ radical also emerges, which may serve as a key precursor for the formation of aromatic rings or polyynes,[55,56] which will be discussed further. These two compounds are considered crucial precursors of carbon inception.[30]

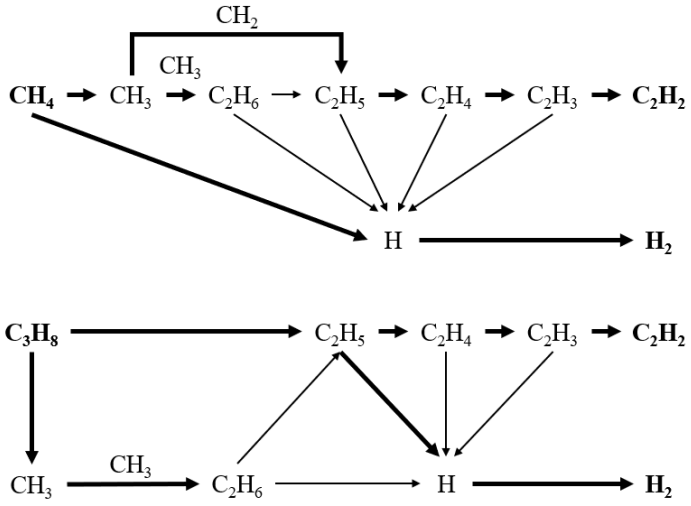


Fig. 4. Reaction pathways leading to $H_2$ and $C_2H_2$ generation in $CH_4$ and $C_3H_8$ systems (the bold arrow from A to B indicates the primary reaction route for the formation of B, where A is the reactant and B is the product).

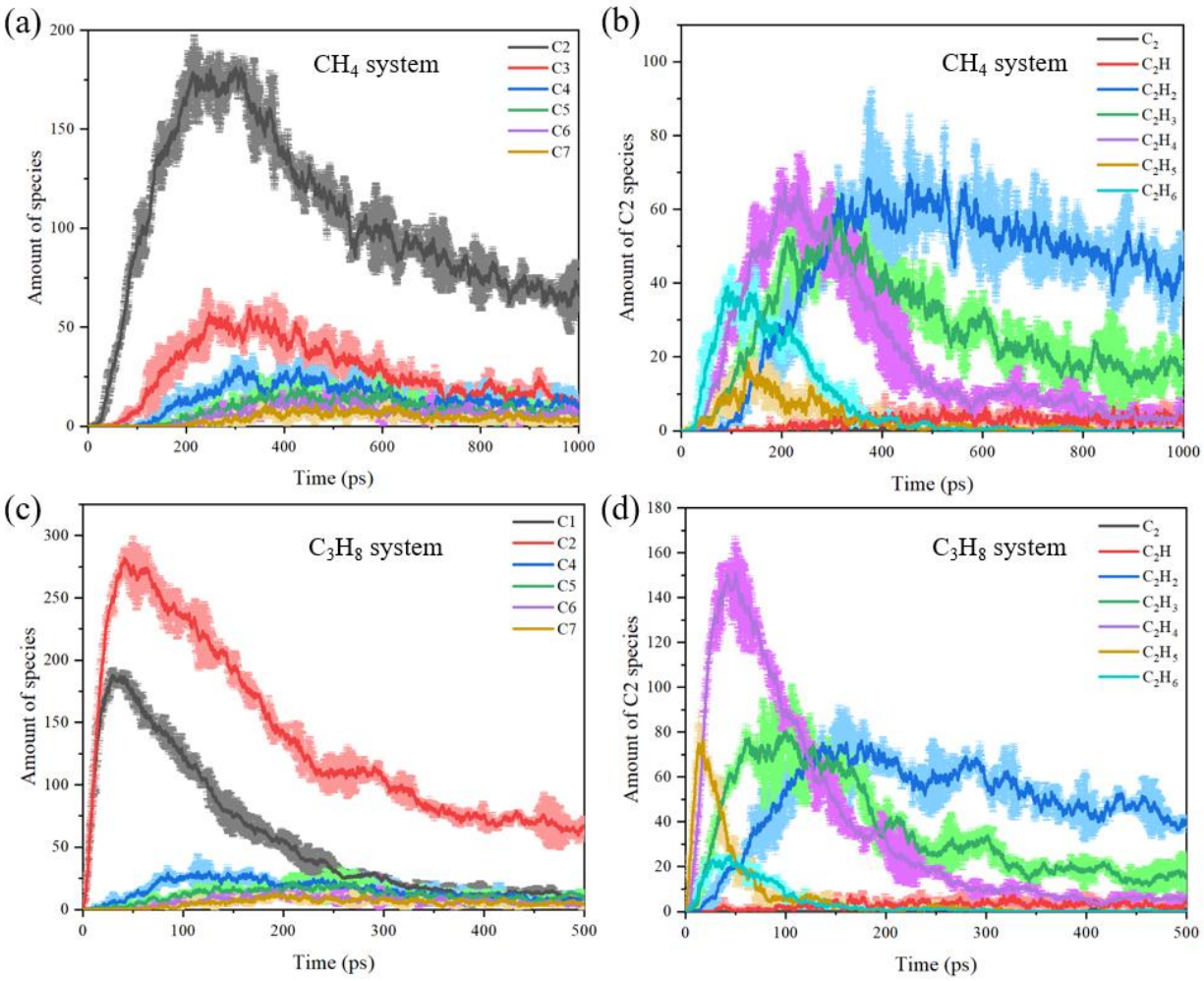


Fig. 5. Evolution of key species during the initial dissociation stage of $CH_4$ and $C_3H_8$ pyrolysis at 3500 K. (a) Formation of carbon-containing species in the $CH_4$ system; (b) Formation of $C_2H_x$ species in the $CH_4$ system; (c) Formation of carbon-containing species in the $C_3H_8$ system; (d) Formation of $C_2H_x$ species in the $C_3H_8$ system.

In Fig. 5c, the simultaneous increase in the amounts of C1 and C2 species indicates initial C–C bond cleavage in the $C_3H_8$ system, which produces equimolar amounts of $CH_3$ and $C_2H_5$ radicals. As the reaction progresses, the amount of C2 species surpasses that of C1 species, primarily due to the recombination of two C1 species to form a C2 species (as shown in Fig 4). This pathway contributes to the continued accumulation of C2 species and a corresponding decline in C1 species. Eventually, the amounts of both C1 and C2 species decrease as carbon atoms are incorporated into larger hydrocarbon structures, a trend consistent with observations in the $CH_4$ system. In Fig 5d, the amount of $C_2H_5$ increases initially due to the primary dissociation of $C_3H_8$. Concurrently, $C_2H_4$ rises rapidly, driven by further C–H bond cleavage in $C_2H_5$ or its participation in hydrogen abstraction reactions. Over time, the number density of $C_2H_4$ surpasses that of $C_2H_5$, reflecting the higher reactivity of the $C_2H_5$ radical and the relative stability of $C_2H_4$. Ultimately, all C2 species—except $C_2H_2$—are rapidly depleted. In contrast, $C_2H_2$ remains at a relatively elevated level, which can be attributed to its higher stability at high temperatures compared to other C2 species.[57]

*3.3. The formation process of carbon clusters*

Carbon formation, an intrinsic outcome of hydrocarbon pyrolysis, represents the final state of the carbon element within hydrocarbons. Unlike $H_2$ formation, which is primarily driven by an increase in entropy, the formation of solid carbon is governed by enthalpic effects.[55] To better understand the carbon cluster growth process, a series of representative snapshots is presented in Fig. 6. In the $CH_4$ system (Fig. 6a), the feedstock initially dissociates to generate multiple $CH_3$ radicals, which subsequently recombine to form C2 species. These C2 intermediates then react with other carbon-containing molecules to produce larger carbon structures. As the number of carbon atoms increases, carbon chains form, then elongate and branch. Afterwards,

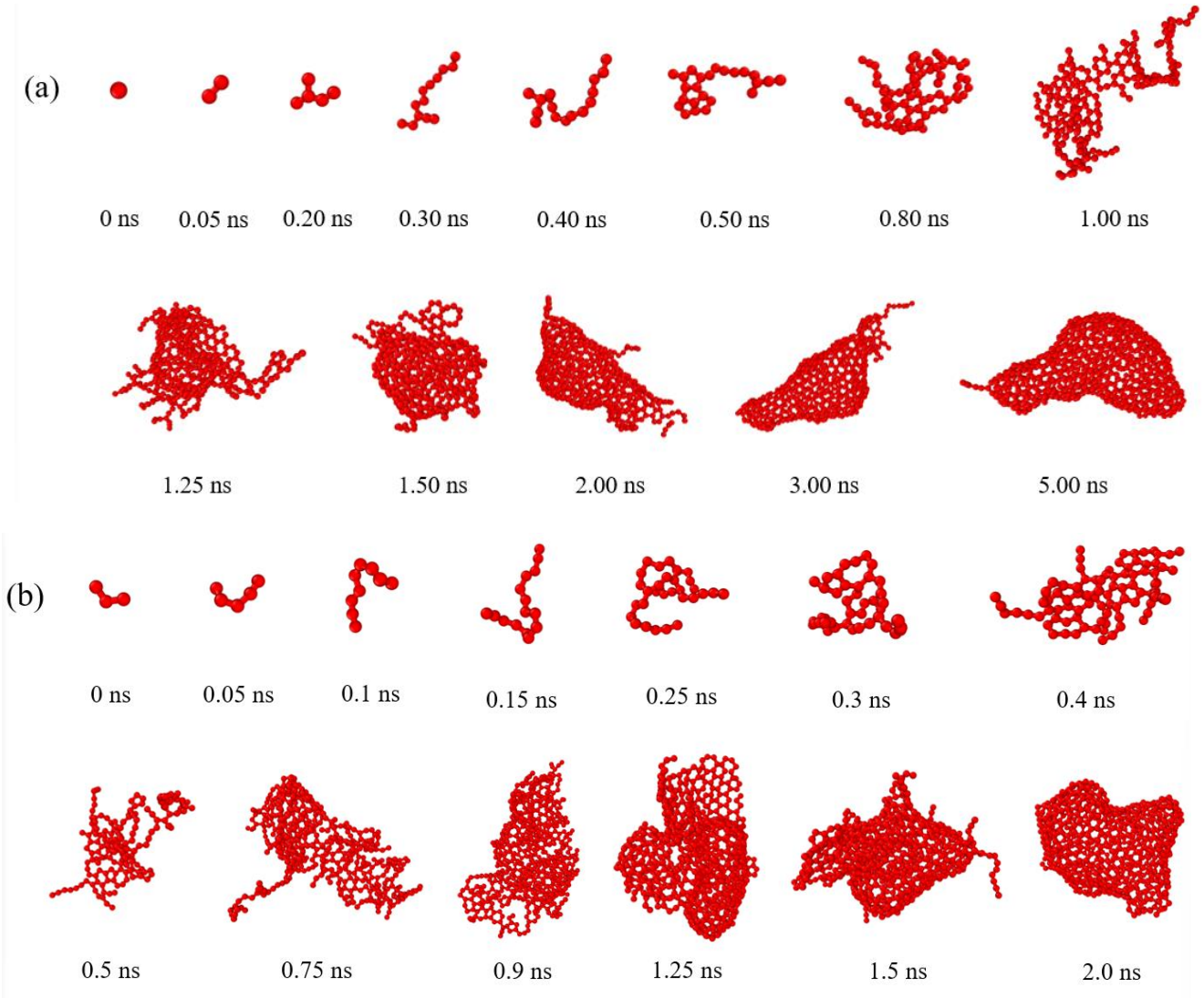


Fig. 6. Sequential snapshots of carbon cluster evolution in (a) $CH_4$ and (b) $C_3H_8$ pyrolysis. H atoms are hidden for better visualization.

as the carbon cluster increases in size, it undergoes sheeting and curling, forming a large number of aromatic rings at its center. Simultaneously, non-aromatic carbon atoms in the periphery of the carbon cluster also react with carbon-containing species to form additional aromatic rings. During this evolution, the formation of five-membered rings can induce curvature in the structure, ultimately leading to the closure of the carbon cluster into a fullerene-like or cage structure. Once a closed structure is established, the growth rate of the carbon cluster decreases markedly due to the limited availability of reactive sites within its surface, which also contributes to the stabilization of the resulting carbon cluster in the simulation.

In the $C_3H_8$ pyrolysis system, the carbon formation process closely resembles that observed in $CH_4$ pyrolysis. However, the presence of C3 species as initial building blocks accelerates the rate of carbon cluster formation. Our simulations reveal that carbon clusters of comparable size (~80 C) form approximately 300 ps faster in the $C_3H_8$ system than in the $CH_4$ system. Overall, the carbon formation process in both systems can be summarized as follows:

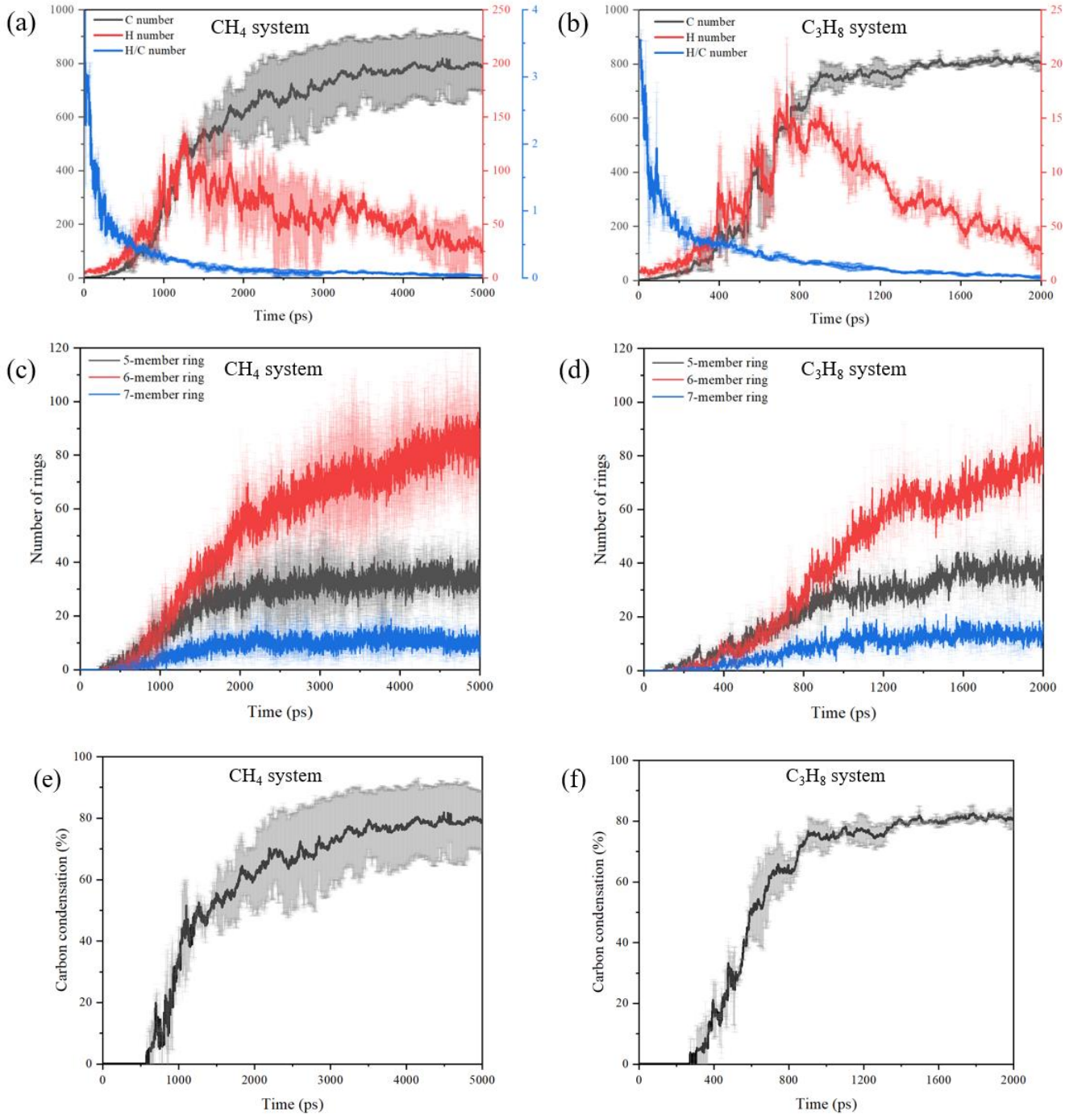


Fig. 7. Time evolution of (a, b) the number of carbon atoms, H atoms, and the H/C ratio within the largest carbon cluster, (c, d) the number of rings, and (e, f) the carbon condensation ratio in $CH_4$ and $C_3H_8$ systems, respectively. All data were collected at a temperature of 3500 K.

(i) a continuous process of entropically driven $H_2$ formation, enriching the carbon species.

(ii) the growth of carbon species, including carbon chain formation, elongation, and branching through C–C coupling.

(iii) the aromatization/graphitization of carbon clusters, accompanied by atomic rearrangements that promote the formation of stable aromatic rings and lead to the stabilization of the clusters.

To quantitatively analyze the carbon cluster formation process, statistical data on the largest carbon cluster and the carbon condensation rate as functions of time are collected and presented in Fig. 7 for both $CH_4$ and $C_3H_8$ pyrolysis systems. In both cases, the number of carbon atoms in the largest cluster follows a similar evolution pattern (Figs. 7a and 7b). Based on the differences in carbon growth rates, the overall process can be divided into three distinct stages. In the first stage, the carbon number increases very slowly, primarily due to: (i) the high energy barrier required to break the stable feedstock molecules, and (ii) the stepwise hydrogen abstraction or dehydrogenation processes needed to form carbon backbones such as $C_2H_2$ and $C_2H$, which serve as precursors for further growth. In the second stage, the accumulation of reactive, large carbon-containing species—characterized by large collision cross-sections and high reactivity—leads to a rapid increase in cluster size. For example, in the $CH_4$ system, the average carbon growth rate from 0.5 to 1.5 ns is 500 ± 50 C/ns, which is much higher than the 80 ± 40 C/ns observed during the first 0.5 ns. In the final stage, the growth rate of the carbon cluster decreases as the number of free carbon species in the simulation box becomes limited. Concurrently, atomic rearrangements within the cluster promote aromatization, which eliminates most active sites and drives the carbon cluster toward a saturated and more stable state.

Notably, the number of H atoms within the carbon clusters initially increases as the cluster grows. Subsequently, it decreases, suggesting that the carbon clusters not only lose hydrogen but also temporarily gain hydrogen atoms via reactions with H-containing species. However, the H/C ratio in the largest carbon cluster consistently decreases over time, indicating the continuous progression of dehydrogenation reactions. In parallel, a continuous increase in the number of six-membered rings is observed (Figs. 7c and 7d). This behavior is characteristic of the aromatization/graphitization process, where dehydrogenation and ring formation proceed in parallel, contributing to the structural evolution toward more stable graphene-based materials. Such a time-dependent feature also indicates that a longer residence time is expected to promote the formation of more stable solid carbon due to enhanced structural ordering. In addition, the emergence of five- and seven-membered rings suggests the development of curvature in the cluster structure, which aligns with the morphological evolution observed in Fig. 6.

The carbon condensation rate was quantitatively analyzed and is shown in Figs. 7e and 7f. In this analysis, carbon-containing species comprising more than 80 carbon atoms (corresponding to a molecular mass of approximately 1000 Da) were classified as solid carbon, representing the threshold for the transition from molecules to carbonaceous nanoparticles.[30] The carbon condensation ratio was defined as the fraction of the number of carbon atoms incorporated into solid carbon to the total number of carbon atoms present in the system. As shown, carbon condensation begins at approximately 580 ps in the $CH_4$ pyrolysis system and around 280 ps in the $C_3H_8$ pyrolysis system. This difference reflects the differing carbon condensation rates between the two systems, consistent with earlier observations. As pyrolysis time increases, the carbon condensation ratio rises sharply, indicating again that carbon formation in hydrocarbon pyrolysis requires a minimum residence time to proceed efficiently.

### *3.4. Discussion of carbon nucleation*

Nucleation remains one of the least understood stages in the overall carbon formation process, due to the challenges associated with experimental detection. Models, such as the $C_2$ condensation theory and the $C_2H_2$ mechanism, were initially proposed;[58,59] however, these frameworks fall short in accounting for the formation of H-containing soot and tend to underestimate the overall carbon production rate.[3,30] In response, alternative mechanisms—including the polyyne and Polycyclic Aromatic Hydrocarbon (PAH)-based theories—have been proposed and have gained prominence.[60,61] The polyyne inception theory, an extension of the $C_2H_2$ mechanism, suggests that carbon nucleation begins with $C_2H_2$, which forms polyynes as intermediate species. These polyynes then undergo polymerization to yield nucleated carbon. This pathway is supported by experimental evidence showing substantial concentrations of polyynes in flame environments and confirming their thermal stability at elevated temperatures.[56,57] In contrast, PAH-based theories propose that the formation of PAHs constitutes the critical step in carbon nucleation. This mechanism is currently the most widely accepted, supported by extensive experimental validation across various combustion systems. The thermal stability and carbon propensity of PAHs make them ideal precursors for carbon formation, reinforcing their central role in the nucleation process.[30]

Our simulation results present a combination of polyyne and PAH-based mechanisms, each dominating at different stages of carbon formation. As shown in Figs. 5b and 6a ($CH_4$ system), when $C_2H_2$ concentration becomes sufficiently high (after 0.3 ns), carbon chains (polyynes) first form and subsequently coagulate into branched structures and larger carbon clusters, rather than forming aromatic rings initially. This phenomenon indicates a polyyne mechanism-dominated process in the early stages of carbon nucleation. The absence of aromatic rings at this stage highlights the superior thermal stability of polyynes compared to small aromatic molecules such as benzene, naphthalene, and pyrene at high temperatures (>2000 K), which is consistent with a previous report.[57] In addition, this process circumvents one of the key limitations of PAH-based theories, which is their relatively slow reaction rates. Furthermore, as carbon clusters grow to approximately 60-80 carbon atoms, aromatization occurs (see Fig. 8), as conjugation stability at high temperatures can only be achieved when a sufficient number of aromatic rings are formed. This process suggests that the PAH-based mechanism starts to dominate at a later stage of carbon nucleation.

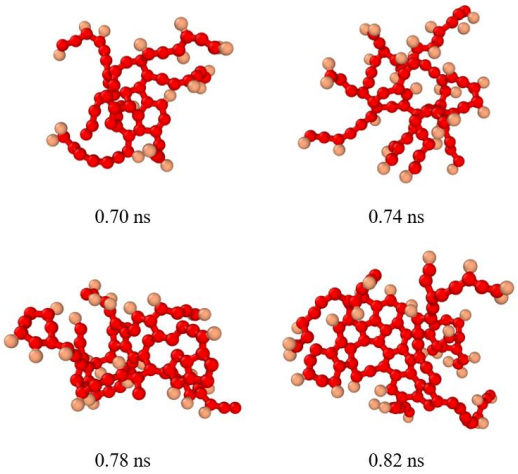


Fig. 8. Rearrangement of carbon atoms within a carbon cluster in the $CH_4$ system (0.1 g/cm$^3$).

However, the early polyyne inception theory faces another notable challenge: recent studies have shown that polyyne size rarely exceeds 150 Da, primarily due to radical-induced fragmentation.[62] Consequently, long polyynes (C > 16) are thermodynamically unfavorable in radical-rich environments and tend to decompose into smaller species such as $C_2H_2$ and C4 fragments, thereby hindering their polymerization into larger carbon structures.[63] However, this degradation pathway was not observed in our simulations, where long carbon chains (C > 4) are frequently encountered. This discrepancy may be attributed to the elevated pressure conditions applied in our simulations, which likely suppress polyyne fragmentation. Furthermore, it suggests that the driving mechanism of carbon nucleation depends on the reaction conditions, with the PAH mechanism being more feasible at low densities and low temperatures, and the polyyne mechanism dominating at high densities and high temperatures. To validate this hypothesis, an additional $CH_4$ pyrolysis simulation was conducted under a lower-density condition (0.01 g/cm$^3$), with the results presented in Fig. 9. As shown, compared with the high-density case, the formation of aromatic rings in the lower-density system occurs when the carbon cluster is relatively smaller. This observation suggests that the PAH-based mechanism becomes dominant at an earlier stage under low-density conditions, thereby supporting our hypothesis.

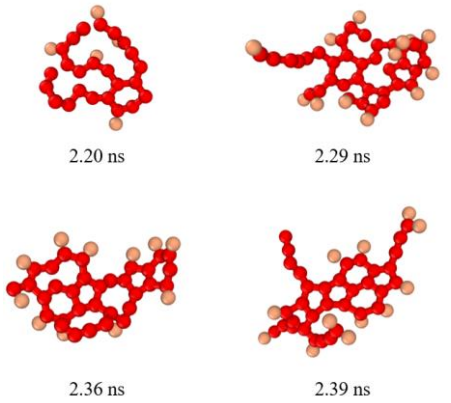


Fig. 9. Aromatic rings formation in the lower-density system (0.01 g/cm$^3$).

Another point warranting attention is that the formation and growth of rings observed in our simulations differ from the mechanisms commonly reported, such as the cyclization of C2 or C3 species. In our case, ring formation is more likely to occur in the central region of the carbon cluster, where the local carbon atom density is higher. This behavior has also been reported in several other ReaxFF-MD simulation studies, in which high temperatures and densities were used to accelerate the reactions.[41-44,64] From both thermodynamic and kinetic perspectives, this process is plausible under high-temperature and high-density conditions: (i) higher carbon density facilitates the formation of larger coagulated structures, which enhances stability, and (ii) ring formation in this environment does not require significant bending or torsion of carbon chains, which would otherwise involve high energy barriers.

In summary, our calculation results suggest that the dominant mechanism of carbon nucleation is determined by the competition between the polyyne and PAH mechanisms—and this competition, in turn, depends on the applied reaction conditions and nucleation stages. Specifically, the PAH theory becomes dominant at an earlier stage of the carbon nucleation process as the applied density/pressure decreases. In reality, the gliding arc plasma source used in our ongoing research operates at atmospheric pressure, with center gas temperatures reaching 3000–4000 K or even higher.[65] Although the detailed carbon nucleation mechanism in such plasma systems remains to be fully elucidated, the atmospheric-pressure nature of the system indicates that the carbon nucleation pathway is likely closer to a PAH-dominated mechanism. With respect to high-pressure reactors, it should be noted that although many practical combustion devices operate under elevated pressures, our current understanding of carbon nucleation mechanisms remains largely derived from studies conducted at atmospheric pressure.[66] Under high-pressure conditions, most experimental investigations have primarily focused on the morphological and structural characterization of the resulting carbon materials, rather than on the early-stage nucleation mechanisms themselves. For instance, Hafiz *et al.* reported that increasing pressure leads to larger soot particle sizes, while Mario *et al.* observed enhanced soot maturity with increasing pressure.[67,68] As a result, the carbon nucleation mechanism under high-pressure conditions remains insufficiently understood. It would be interesting to experimentally verify the early-stage carbon nucleation predicted by our high-density, high-temperature simulations, which support a polyyne-based mechanism under such conditions.

## Conclusions

This study employed ReaxFF-MD simulations to investigate the atomic-scale co-production of clean $H_2$ and value-added carbon during high-temperature, high-density pyrolysis of $CH_4$ and $C_3H_8$. The analysis focused on decomposition kinetics, gaseous product evolution, and carbon formation mechanisms.

The kinetic analysis demonstrates that $C_3H_8$ decomposes significantly faster than $CH_4$, attributed to its weaker C–C bonds. Regarding initial decomposition pathways, hydrogen abstraction reactions dominate in the $CH_4$ system, whereas C–C bond cleavage is more prominent in the $C_3H_8$ system, influencing subsequent reaction routes and product distributions.

$H_2$ production in both $CH_4$ and $C_3H_8$ pyrolysis systems primarily proceeds through hydrogen abstraction reactions involving early-formed H radicals. $C_2H_2$ formation follows a stepwise dehydrogenation pathway of C2 intermediates. $CH_4$ exhibits higher initial $H_2$ selectivity due to the early generation of H radicals, while $C_3H_8$ shows a delayed yet steadily increasing $H_2$ production profile. $C_2H_2$ selectivity analysis reveals that $CH_4$ requires higher temperatures or longer reaction times to initiate $C_2H_2$ formation, involving more complex pathways. In contrast, $C_3H_8$ facilitates earlier $C_2H_2$ generation through the formation of $C_2H_5$ intermediates.

Carbon cluster growth was characterized by three distinct stages: (i) fragmentation of feedstock molecules; (ii) growth involving elongation and branching of carbon chains, and (iii) aromatization/graphitization, marked by aromatic rings formation, hydrogen elimination, and structural stabilization. Between the two systems, $C_3H_8$ exhibited a higher carbon condensation rate than $CH_4$.

The carbon nucleation mechanisms observed in the simulations can be explained by the polyyne and PAH-based inception theories, as well as by high temperature and high-density conditions applied. Specifically, in our simulations, the polyyne-based mechanism dominates the early stage of carbon nucleation, whereas the PAH-based mechanism prevails at later stages. Considering the relative stability of these two intermediates under different conditions, we suggest the PAH pathway is likely favored at low densities and temperatures. In contrast, the polyyne pathway tends to dominate at high densities and high temperatures.

Overall, this study advances our understanding of light hydrocarbon pyrolysis, thereby complementing our ongoing efforts to

elucidate the complex reaction pathways in plasma-assisted processes. Furthermore, the results also highlight the utility of the ReaxFF-MD method in capturing complex reaction networks and structural transformations at the atomic scale, reinforcing its role as a predictive tool for modeling hydrocarbon pyrolysis under diverse conditions. Finally, the proposed polyyne-dominated mechanism for early-stage carbon nucleation at high densities and temperatures emphasizes the importance of experimental verification, which could offer novel insights into carbon nucleation under extreme conditions.

## CRediT authorship contribution statement

**Yuan Tian:** Writing– review & editing, Writing– original draft, Methodology, Investigation, Formal analysis, Data curation, Visualization, Conceptualization. **Nathalie De Geyter:** Writing– review & editing, Supervision, Funding acquisition. **Carla Bittencourt:** Writing review & editing, Supervision, Conceptualization. **Chris Ewels:** Investigation, writing review & editing. **Rony Snyders:** Writing review & editing, Supervision, Funding acquisition, Conceptualization.

## Declaration of competing interest

The authors declare that they have no known competing financial interests or personal relationships that could have appeared to influence the work reported in this paper.

## Data availability

Data will be made available on request.

## Acknowledgements

This research is supported by the Excellence of Science FWO-FNRS project (PLASyntH2, FNRS grant O.0023.22, EOS I: 40007511). Computational resources have been provided by the Consortium des Équipements de Calcul Intensif (CÉCI), funded by the Fonds de la Recherche Scientifique de Belgique (F.R.S.-FNRS) under Grant No. 2.5020.11 and by the Walloon Region.

## References

[1] Ball, M., & Wietschel, M. (2009). The future of $H_2$—Opportunities and challenges. International Journal of Hydrogen Energy, 34(2), 615–627.

[2] International Energy Agency (IEA). Global $H_2$ Review 2025; International Energy Agency: Paris, France, 2025. https://www.iea.org/reports/global-$H_2$-review-2025 (accessed 2026-01-20).

[3] Donnet, J. B., Bansal, R. C., & Wang, M. (1993). Carbon Black: Science and Technology. Boca Raton: CRC Press.

[4] Prabowo, J., Lai, L., Chivers, B., Burke, D., Dinh, A. H., Ye, L., ... & Chen, Y. (2024). Solid carbon co-products from hydrogen production by methane pyrolysis: Current understandings and recent progress. Carbon, 216, 118507.

[5] Fulcheri, L., Dames, E., & Rohani, V. (2024). Plasma-based conversion of $CH_4$ into $H_2$ and carbon black. Current Opinion in Green and Sustainable Chemistry, 50, 100973.

[6] Patlolla, S. R., Katsu, K., Sharafian, A., Wei, K., Herrera, O. E., & Mérida, W. (2023). A review of methane pyrolysis technologies for hydrogen production. Renewable and Sustainable Energy Reviews, 181, 113323.

[7] Zhang, H., Du, C., Wu, A., Bo, Z., Yan, J., & Li, X. (2014). Rotating gliding arc assisted methane decomposition in nitrogen for hydrogen production. International journal of hydrogen energy, 39(24), 12620-12635.

[8] Ogihara, H., Tajima, H., & Kurokawa, H. (2020). Pyrolysis of mixtures of methane and ethane: Activation of methane with the aid of radicals generated from ethane. Reaction Chemistry & Engineering, 5(1), 145–153.

[9] Zheng, Y., Tao, L., Yang, X., Huang, Y., Liu, C., & Zheng, Z. (2018). Study of the thermal behavior, kinetics, and product characterization

of biomass and low-density polyethylene co-pyrolysis by thermogravimetric analysis and pyrolysis-GC/MS. Journal of Analytical and Applied Pyrolysis, 133, 185-197.

[10] Fulcheri, L., Rohani, V. J., Wyse, E., Hardman, N., & Dames, E. (2023). An energy-efficient plasma methane pyrolysis process for high yields of carbon black and hydrogen. International journal of hydrogen energy, 48(8), 2920-2928.

[11] Dadsetan, M., Latham, K. G., Khan, M. F., Zaher, M. H., Manzoor, S., Bobicki, E. R., ... & Thomson, M. J. (2023). Characterization of carbon products from microwave-driven methane pyrolysis. Carbon Trends, 12, 100277.

[12] Tian, Y., Abdirakhmanov, A., Wang, X., Mathieu, P., Flores-Larrea, L., Lagos, M. J., ... & Snyders, R. (2025). Synthesis of carbon-based materials by methane pyrolysis in a low-current gliding arc discharge. Surface and Coatings Technology, 505, 132063.

[13] Kang, J., Ran, J., Niu, J., Shi, J., He, J., & Yang, Z. (2019). Experimental and theoretical study on propane pyrolysis to produce gas and soot. International Journal of Hydrogen Energy, 44(41), 22904-22918.

[14] Sun, D. L., Wang, F., Hong, R. Y., & Xie, C. R. (2016). Preparation of carbon black via arc discharge plasma enhanced by thermal pyrolysis. Diamond and Related Materials, 61, 21-31.

[15] Sun, D. L., Hong, R. Y., Liu, J. Y., Wang, F., & Wang, Y. F. (2016). Preparation of carbon nanomaterials using two-group arc discharge plasma. Chemical Engineering Journal, 303, 217-230.

[16] Hidaka, Y., Sato, K., Hoshikawa, H., Nishimori, T., Takahashi, R., Tanaka, H., ... & Ito, N. (2000). Shock-tube and modeling study of ethane pyrolysis and oxidation. Combustion and flame, 120(3), 245-264.

[17] Nativel, D., Shu, B., Herzler, J., Fikri, M., & Schulz, C. (2019). Shock-tube study of methane pyrolysis in the context of energy-storage processes. Proceedings of the Combustion Institute, 37(1), 197-204.

[18] Layokun, S. K., & Slater, D. H. (1979). Mechanism and kinetics of propane pyrolysis. Industrial & Engineering Chemistry Process Design and Development, 18(2), 232–236.

[19] Bradley, J. N. (1979). Single-pulse shock tube studies of hydrocarbon pyrolysis. Part 7—Pyrolysis of propane. Journal of the Chemical Society, Faraday Transactions 1, 75, 2819–2826.

[20] Al-Alami, M. Z., & Kiefer, J. H. (1983). Shock-tube study of propane pyrolysis. Rate of initial dissociation from 1400 to 2300 K. Journal of Physical Chemistry, 87(3), 499–506.

[21] Oehlschlaeger, M. A., Davidson, D. F., & Hanson, R. K. (2005). High-temperature ethane and propane decomposition. Proceedings of the Combustion Institute, 30(1), 1119–1127.

[22] Koike, T., & Gardiner, W. C. Jr. (1980). Thermal decomposition of propane. Journal of Physical Chemistry, 84(16), 2005–2009.

[23] Aldén, M., Bood, J., Li, Z., & Richter, M. (2011). Visualization and understanding of combustion processes using spatially and temporally resolved laser diagnostic techniques. Proceedings of the Combustion Institute, 33(1), 69-97.

[24] Starke, R., & Roth, P. (2001). Soot particle sizing by LII during shock tubepyrolysis of $C_6H_6$. Combustion and flame, 127(4), 2278-2285.

[25] Utsav, K. C., Beshir, M., & Farooq, A. (2017). Simultaneous measurements of acetylene and soot during the pyrolysis of ethylene and benzene in a shock tube. Proceedings of the Combustion Institute, 36(1), 833–840.

[26] Corchado, J. C., Bravo, J. L., & Espinosa-Garcia, J. (2009). The hydrogen abstraction reaction H + $CH_4$. I. New analytical potential energy surface based on fitting to ab initio calculations. Journal of Chemical Physics, 130(18), 184301.

[27] Kerkeni, B., & Clary, D. C. (2004). Ab initio rate constants from hyperspherical quantum scattering: Application to H + $CH_4$ → $H_2$ + $CH_3$. Journal of Chemical Physics, 120(5), 2308–2318.

[28] Sutherland, J. W., Su, M. C., & Michael, J. V. (2001). Rate constants for H + $CH_4$, $CH_3$ + $H_2$, and $CH_4$ dissociation at high temperature. International Journal of Chemical Kinetics, 33(11), 669–684.

[29] Cavallotti, C., Rota, R., & Carrà, S. (2002). Quantum chemistry computation of rate constants for reactions involved in the first aromatic ring formation. Journal of Physical Chemistry A, 106(34), 7769–7778.

[30] Martin, J. W., Salamanca, M., & Kraft, M. (2022). Soot inception: Carbonaceous nanoparticle formation in flames. Progress in Energy and Combustion Science, 88, 100956.

[31] Mao, Q., Feng, M., Jiang, X. Z., Ren, Y., Luo, K. H., & van Duin, A. C. (2023). Classical and reactive molecular dynamics: Principles and applications in combustion and energy systems. Progress in Energy and Combustion Science, 97, 101084.

[32] Kohse-Höinghaus, K., Barlow, R. S., Aldén, M., & Wolfrum, J. (2005). Combustion at the focus: laser diagnostics and control. Proceedings of the Combustion Institute, 30(1), 89-123.

[33] Van Duin, A. C., Dasgupta, S., Lorant, F., & Goddard, W. A. (2001). ReaxFF: a reactive force field for hydrocarbons. The Journal of Physical Chemistry A, 105(41), 9396-9409.

[34] Chenoweth, K., Van Duin, A. C. T., & Goddard, W. A. (2008). ReaxFF reactive force field for molecular dynamics simulations of hydrocarbon oxidation. Journal of Physical Chemistry A, 112(5), 1040–1053.

[35] Chenoweth, K., Van Duin, A. C., Dasgupta, S., & Goddard Iii, W. A. (2009). Initiation mechanisms and kinetics of pyrolysis and combustion of JP-10 hydrocarbon jet fuel. The Journal of Physical Chemistry A, 113(9), 1740-1746.

[36] Bharti, A., & Banerjee, T. (2016). Reactive force field simulation studies on the combustion behavior of n-octanol. Fuel Processing Technology, 152, 132–139.

[37] Gao, M., Li, X., & Guo, L. (2018). Pyrolysis simulations of Fugu coal by large-scale ReaxFF molecular dynamics. Fuel Processing Technology, 178, 197–205.

[38] Zhang, M., Zhou, B., Chen, Y., & Gong, H. (2022). Mechanism and safety analysis of acetylene decomposition explosion: A combined ReaxFF MD with DFT study. Fuel, 327, 124996.

[39] Yang, Y., Kai, R., & Watanabe, H. (2024). Reaction mechanism and light gas conversion in pyrolysis and oxidation of dimethyl ether (DME, $C_2H_6O$): A ReaxFF molecular dynamics study. Energy, 295, 131013.

[40] Ashraf, C., & Van Duin, A. C. T. (2017). Extension of the ReaxFF combustion force field toward syngas combustion and initial oxidation kinetics. Journal of Physical Chemistry A, 121(5), 1051–1068.

[41] Lümmen, N. (2010). ReaxFF molecular dynamics simulations of non-oxidative and non-catalyzed thermal decomposition of $CH_4$ at high temperatures. Physical Chemistry Chemical Physics, 12(28), 7883–7893.

[42] Xue, X., Meng, L., Ma, Y., & Zhang, C. (2017). Molecular reactive force-field simulations on the carbon nanocavities from methane pyrolysis. The Journal of Physical Chemistry C, 121(13), 7502-7513.

[43] Liu, J., Ke, H., Zhong, K., He, X., Xue, X., Wang, L., & Zhang, C. (2018). Higher activity leading to higher disorder: a case of four light hydrocarbons to variable morphological carbonaceous materials by pyrolysis. The Journal of Physical Chemistry C, 122(51), 29516-29525.

[44] Ganguly, A., Mukut, K. M., Roy, S., Kelesidis, G., & Goudeli, E. (2025). Investigation of soot precursor molecules during inception by acetylene pyrolysis using reactive molecular dynamics. Aerosol Research, 3(1), 185-203.

[45] Huo, E., Xu, D., Wang, S., & Chen, Y. (2023). Thermal decomposition mechanism and thermal stability prediction of n-pentane/n-butane mixture. Energy, 284, 128585.

[46] Aktulga, H. M., Fogarty, J. C., Pandit, S. A., & Grama, A. Y. (2012). Parallel reactive molecular dynamics: Numerical methods and algorithmic techniques. parallel computing, 38(4-5), 245-259.

[47] Stukowski, A. (2009). Visualization and analysis of atomistic simulation data with OVITO—the Open Visualization Tool. Modelling and Simulation in Materials Science and Engineering, 18(1), 015012.

[48] Zeng, J., Cao, L., Chin, C. H., Ren, H., Zhang, J. Z., & Zhu, T. (2020). ReacNetGenerator: an automatic reaction network generator for reactive molecular dynamics simulations. Physical chemistry chemical physics, 22(2), 683-691.

[49] Wang, Y., Hu, P., Yang, J., Zhu, Y. A., & Chen, D. (2021). C–H bond activation in light alkanes: a theoretical perspective. Chemical Society Reviews, 50(7), 4299-4358.

[50] Kozlov G I, Knorre V G. Single-pulse shock tube studies on the kinetics of the thermal decomposition of methane[J]. Combustion and Flame, 1962, 6: 253-263.

[51] Schobert, H. (2014). Production of $C_2H_2$ and $C_2H_2$-based chemicals from coal. Chemical Reviews, 114(3), 1743–1760.

[52] Wang, H., Xu, R., Wang, K., Bowman, C. T., Hanson, R. K., Davidson, D. F., ... & Egolfopoulos, F. N. (2018). A physics-based approach to modeling real-fuel combustion chemistry-I. Evidence from experiments, and thermodynamic, chemical kinetic and statistical considerations. Combustion and Flame, 193, 502-519.

[53] Weissman, M., & Benson, S. W. (1989). Mechanism of soot initiation in $CH_4$ systems. Progress in Energy and Combustion Science, 15(4), 273–285.

[54] McEnally, C. S., Pfefferle, L. D., Atakan, B., & Kohse-Höinghaus, K. (2006). Studies of aromatic hydrocarbon formation mechanisms in flames: Progress towards closing the fuel gap. Progress in Energy and Combustion Science, 32(3), 247-294.

[55] Richter, H., & Howard, J. B. (2000). Formation of polycyclic aromatic hydrocarbons (PAHs) and their growth to soot—A review of chemical reaction pathways. Progress in Energy and Combustion Science, 26(4–6), 565–608.

[56] Krestinin, A. V. (2000). Detailed modeling of soot formation in hydrocarbon pyrolysis. Combustion and Flame, 121(3), 513–524.

[57] Krestinin, A. V. (1998). Polyyne model of soot formation process. Proceedings of the 27th International Symposium on Combustion. Amsterdam: Elsevier, 1–8.

[58] Palmer, H. B., & Cullis, C. F. (1965). The formation of carbon from gases. Proceedings of the Combustion Institute, 1, 265–325.

[59] Porter, G. (1953). Carbon formation in the combustion wave. Proceedings of the 4th International Symposium on Combustion. Amsterdam: Elsevier, 1–10.

[60] Homann, K. H., & Wagner, H. G. (1967). Some new aspects of the mechanism of carbon formation in premixed flames. Proceedings of the 11th International Symposium on Combustion. Amsterdam: Elsevier, 371–379.

[61] Rummel, K., & Veh, P. O. (1941). Die Strahlung leuchtender Flammen. Erster Teil: Schrifttumsgrundlagen, Arbeitshypothesen und Vorversuche. Archiv für das Eisenhüttenwesen, 14(10), 489–499.

[62] Gerhardt, Ph., & Homann, K. H. (1990). Ions and charged soot particles in hydrocarbon flames. 2. Positive aliphatic and aromatic ions in ethyne/oxygen flames. Journal of Physical Chemistry, 94(13), 5381–5391.

[63] Hansen, N., Jensen, A., & Kohse-Höinghaus, K. (2009). Recent contributions of flame-sampling molecular-beam mass spectrometry to a fundamental understanding of combustion chemistry. Progress in Energy and Combustion Science, 35(2), 168–191.

[64] Han, S., Li, X., Nie, F., Zheng, M., Liu, X., & Guo, L. (2017). Revealing the initial chemistry of soot nanoparticle formation by ReaxFF molecular dynamics simulations. Energy & Fuels, 31(8), 8434-8444.

[65] Böddeker, S., Göricke, J., Kogelheide, B., Bibinov, N., Purcel, M., Muhler, M., ... & Awakowicz, P. (2025). Characterization of a Gliding Arc Plasmatron for the Plasma Assisted Pyrolysis of Methane to Acetylene and Hydrogen. Plasma Processes and Polymers, 22(3), 2400250.

[66] Karataş, A. E., & Gülder, Ö. L. (2012). Soot formation in high pressure laminar diffusion flames. Progress in Energy and Combustion Science, 38(6), 818-845.

[67] Commodo, M., Karataş, A. E., De Falco, G., Minutolo, P., D'Anna, A., & Gülder, Ö. L. (2020). On the effect of pressure on soot nanostructure: A Raman spectroscopy investigation. Combustion and Flame, 219, 13-19.

[68] Amin, H. M., Bennett, A., & Roberts, W. L. (2019). Determining fractal properties of soot aggregates and primary particle size distribution in counterflow flames up to 10 atm. Proceedings of the Combustion Institute, 37(1), 1161-1168.

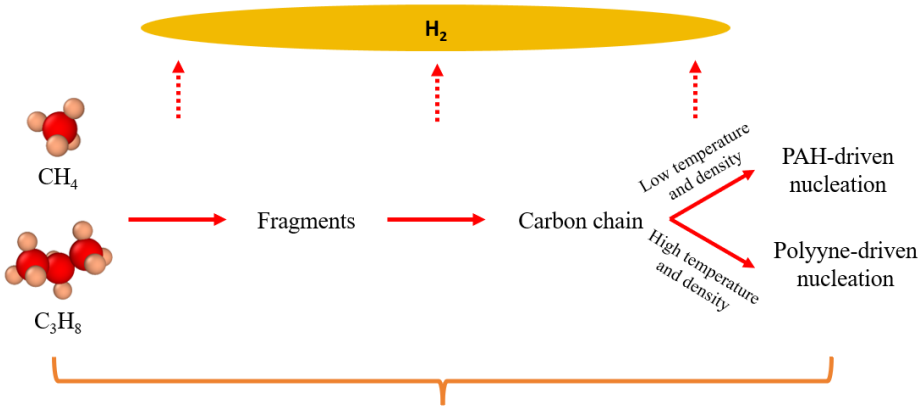


ReaxFF-MD simulation of light hydrocarbons pyrolysis

TOC Graphic